# **Adhesive Anti-fibrotic Interfaces on Diverse Organs**

Jingjing Wu<sup>1</sup>, Jue Deng<sup>1</sup>, Georgios Theocharidis<sup>2</sup>, Tiffany L. Sarrafian<sup>3</sup>, Leigh G. Griffiths<sup>4</sup>, Roderick T. Bronson<sup>5</sup>, Aristidis Veves<sup>2</sup>, Jianzhu Chen<sup>6</sup>, Hyunwoo Yuk<sup>1,8</sup>\*, Xuanhe Zhao<sup>1,7</sup>\*

Implanted biomaterials and devices face compromised functionality and efficacy in the long term due to foreign body reactions and subsequent formation of fibrous capsules at the implant-tissue interfaces 1-4. Here, we demonstrate that an adhesive implant-tissue interface can mitigate fibrous capsule formation in diverse animal models, including rats, mice, humanized mice, and pigs, by reducing the infiltration of inflammatory cells into the adhesive implant-tissue interface compared to the non-adhesive implant-tissue interface. Histological analysis shows that the adhesive implant-tissue interface does not form observable fibrous capsules on diverse organs, including the abdominal wall, colon, stomach, lung, and heart, over 12 weeks in vivo. In vitro protein adsorption, multiplex Luminex assays, quantitative PCR, immunofluorescence analysis, and RNA sequencing are additionally performed to validate the hypothesis. We further demonstrate long-term bi-directional electrical communication enabled by implantable electrodes with an adhesive interface over 12 weeks in a rat model in vivo. This finding may offer a promising strategy for long-term anti-fibrotic implant-tissue interfaces.

<sup>&</sup>lt;sup>1</sup> Department of Mechanical Engineering, Massachusetts Institute of Technology, Cambridge, MA, USA

<sup>&</sup>lt;sup>2</sup> Joslin-Beth Israel Deaconess Foot Center and The Rongxiang Xu, MD, Center for Regenerative Therapeutics, Beth Israel Deaconess Medical Center, Harvard Medical School, Boston, MA, USA

<sup>&</sup>lt;sup>3</sup> Department of Thoracic Surgery, Mayo Clinic, Rochester, MN, USA

<sup>&</sup>lt;sup>4</sup> Department of Cardiovascular Medicine, Mayo Clinic, Rochester, MN, USA

<sup>&</sup>lt;sup>5</sup> Department of Immunology, Harvard Medical School, Boston, MA, USA

<sup>&</sup>lt;sup>6</sup> Koch Institute for Integrative Cancer Research and Department of Biology, Massachusetts Institute of Technology, Cambridge, MA, USA

<sup>&</sup>lt;sup>7</sup> Department of Civil and Environmental Engineering, Massachusetts Institute of Technology, Cambridge, MA, USA

<sup>&</sup>lt;sup>8</sup> Present address: SanaHeal, Inc., Cambridge, MA, USA

<sup>\*</sup>Corresponding authors, <u>zhaox@mit.edu</u>; <u>hyunwooyuk@sanaheal.com</u>

Foreign body reactions to implants are among the most critical challenges that undermine the long-term functionality and reliability of biomaterials and devices in vivo<sup>1-4</sup>. In particular, the formation of a fibrous capsule between the implant and the target tissue, as a result of foreign body reactions, can substantially compromise the implant's efficacy because the fibrous capsule acts as a barrier to mechanical, electrical, chemical, or optical communications<sup>4-11</sup> (Fig. 1a,b). To alleviate the formation of the fibrous capsule at the implant-tissue interface, various approaches have been developed, including drug-eluting coatings<sup>12</sup>, hydrophilic<sup>13</sup> or zwitterionic polymer coatings<sup>14-16</sup>, active surfaces<sup>17,18</sup>, and controlling the stiffness<sup>19</sup> and/or size<sup>20,21</sup> of the implants. However, despite recent advances, the mitigation of fibrous capsule formation for implanted biomaterials and devices remains an ongoing challenge in the field<sup>5,22</sup>, highlighting the importance of developing new solutions and strategies.

Here, we demonstrate that an adhesive interface can not only provide mechanical integration of the implant with the target tissue but also prevent the formation of observable fibrous capsules at the implant-tissue interface (Fig. 1c,d). We hypothesize that the conformal interfacial integration between the adhesive implant and the tissue surface can reduce the infiltration of inflammatory cells (e.g., neutrophils, monocytes, macrophages) into the adhesive implant-tissue interface, resulting in decreased collagen deposition and reduced fibrous capsule formation in the long term (Fig. 1d). In contrast, conventional non-adhesive implants usually do not form conformal integration with the tissue surfaces and attract the infiltration of inflammatory cells into the non-adhesive implant-tissue interfaces. Subsequently, fibrous capsules form on the non-adhesive implant-tissue interfaces (Fig. 1b).

To test our hypothesis, we prepared an adhesive implant consisting of a mock device (polyurethane) and an adhesive layer<sup>23,24</sup> composed of interpenetrating networks between the covalently-crosslinked poly(acrylic acid) *N*-hydroxysuccinimide (NHS) ester and physically-crosslinked poly(vinyl alcohol) (PVA) (Fig. 1c). The adhesive layer provides highly conformal and stable integration of the implant with wet tissues<sup>23-25</sup> (Supplementary Fig. 1). We further prepared a non-adhesive implant by fully swelling the same mock device and adhesive layer in a phosphate-buffered saline (PBS) bath before implantation (see Methods for the preparation of the non-adhesive implant). By swelling the implant in PBS, we removed its adhesive property<sup>26</sup> while keeping its chemical composition identical.

Both adhesive and non-adhesive implants were implanted on the surfaces of diverse organs, including the abdominal wall, colon, stomach, lung, and heart, using rat models in vivo for up to 84 days (Fig. 1e-i). Note that the non-adhesive implant was sutured onto the organ surfaces. Macroscopic observations showed that both adhesive and non-adhesive implants remained stable at the implantation site on the organ surfaces (Extended Data Fig. 1b,c). To analyze the foreign body reaction and fibrous capsule formation for the adhesive and non-adhesive implants, we performed histological analysis of the native tissue, adhesive implant, and non-adhesive implant for various organs (Extended Data Fig. 1a).

Histological evaluation by a blinded pathologist indicates that the adhesive implant forms conformal integration with the organ surface and shows no observable formation of the fibrous

capsule up to 84 days post-implantation for diverse organs, including the abdominal wall, colon, stomach, lung, and heart (Fig. 1e-i, Extended Data Fig. 2, and Supplementary Fig. 2). Furthermore, a transmission electron microscope (TEM) image of the adhesive implant-tissue interface shows that the adhesive layer maintains highly conformal integration with the collagenous layer of the mesothelium on a subcellular scale on day 28 post-implantation (Extended Data Fig. 3). In contrast, the non-adhesive implant undergoes substantial formation of the fibrous capsule at the implant-tissue interface for all organs, consistent with the foreign body reaction to the mock device alone (Fig. 1, Supplementary Figs. 2 and 3). Similarly, the mock device-cavity interface of the adhesive implant undergoes fibrous capsule formation (the top of the implant in Extended Data Fig. 2).

To investigate the potential influence of suture-induced tissue damage, sutures were introduced to the corners of the adhesive implant, similar to those used with the non-adhesive implant (Extended Data Fig. 4a). The histological analysis shows that the suture point exhibits the formation of fibrosis (Extended Data Fig. 4b,c), but the intact adhesive implant-tissue interface demonstrates no observable formation of the fibrotic capsule (Extended Data Fig. 4b,d). Collectively, these data further confirm that the adhesive interface is required to prevent the observable formation of the fibrous capsule.

To investigate the effect of adhesive interfaces with varying compositions and properties, we replaced the PVA-based adhesive interface with a chitosan-based adhesive interface<sup>23</sup> (see Methods for the preparation of the chitosan-based adhesive interface). Compared to the PVA-based adhesive interface, the chitosan-based adhesive interface offers a different composition and Young's modulus, yet it demonstrates comparable adhesion performance (Extended Data Fig. 5a-d). Histological analysis shows that the chitosan-based adhesive interface exhibits no observable formation of the fibrous capsule on day 14 post-implantation (Extended Data Fig. 5e,f). Notably, the implants adhered to the abdominal wall surface using commercially-available tissue adhesives including Coseal and Tisseel show the substantial formation of the fibrous capsule on day 14 post-implantation (Extended Data Fig. 6). This may be attributed to unstable long-term adhesion of the commercially-available tissue adhesives with the tissue surface in vivo<sup>27,28</sup>.

To assess the foreign body reaction and fibrous capsule formation over time, we conducted histological analyses for the adhesive and non-adhesive implants on the abdominal wall on days 3, 7, 14, 28, and 84 post-implantation (Fig. 2a-j). The collagen layer thickness at the implant-tissue interface remains comparable to that of the native tissue (i.e., the mesothelium thickness) for the adhesive implant at all time points (Fig. 2k). In contrast, the collagen layer thickness at the non-adhesive implant-tissue interface increases over time due to the formation of the fibrous capsule and is significantly thicker than that of both the native tissue and the adhesive implant at all time points (Fig. 2k).

To further investigate our hypothesis, we performed a set of characterizations for key participants of the foreign body reaction, including in vitro protein adsorption assays, immunofluorescence analysis, quantitative PCR (qPCR), Luminex quantification, and RNA sequencing analysis. A protein adsorption assay with fluorescently-labeled albumin and fibrinogen

was carried out to evaluate the adhesion of proteins at the implant-tissue interface during the initial stage of the foreign body reaction<sup>29,30</sup> (Supplementary Fig. 4). After 30 minutes of co-culture in the protein solution, the adhesive implant-substrate interface showed significantly lower protein adsorption compared to that of the non-adhesive implant-substrate interface (P < 0.0001) for both fluorescently-labeled albumin and fibrinogen (Supplementary Fig. 4g,h), demonstrating the adhesive interface's capability to prevent protein adsorption.

To investigate the infiltration of immune cells into the implant-tissue interface, we performed immunofluorescence staining for fibroblasts (αSMA), neutrophils (neutrophil elastase), macrophages (CD68 for pan-macrophages; iNOS and vimentin for pro-inflammatory macrophages; CD206 for anti-inflammatory macrophages), and T-cells (CD3) on days 3, 7, and 14 post-implantation (Fig. 3a-f). Quantification of cell numbers in the collagenous layer at the implant-tissue interface over a representative width of 500μm from the immunofluorescence images shows significantly fewer fibroblasts, neutrophils, macrophages, and T-cells at the adhesive implant-tissue interface than at the non-adhesive implant-tissue interface at all time points (Fig. 3g-i).

To further delineate the immune response at the implant-tissue interface, we profile immune cell-related genes and cytokines using qPCR analysis and Luminex quantification, respectively (Fig. 4). On day 3 post-implantation, while the levels of most select immune gene transcripts are similar or significantly lower in the adhesive compared to the non-adhesive implant-tissue interface, the level of *Nos2* is significantly higher in the adhesive than in the non-adhesive implant-tissue interface (Fig. 4b). The higher level of *Nos2* expression is in agreement with the higher levels of inflammatory cytokines (G-CSF, IL-12p70) in the adhesive than the non-adhesive implant-tissue interface on day 3 post-implantation (Fig. 4d and Supplementary Table 1).

To investigate the source of Nos2 on day 3 post-implantation, we performed double immunofluorescence staining for iNOS/neutrophil elastase and iNOS/CD68 (Extended Data Fig. 7). The immunofluorescence staining of the adhesive implant-tissue interface reveals a significantly higher number of iNOS+ neutrophils than iNOS+ macrophages on day 3 post-implantation ( $P \le 0.01$ ) (Extended Data Fig. 7b). In contrast, the non-adhesive implant-tissue interface has similar numbers of iNOS+ neutrophils and iNOS+ macrophages on day 3 post-implantation (P = 0.82) (Extended Data Fig. 7d). This result indicates that the adhesive implant-tissue interface favors an iNOS-producing neutrophil subset on day 3 post-implantation<sup>31</sup>.

By day 7 post-implantation, the adhesive implant-tissue interface exhibits a significantly lower expression of all immune cell-related genes, including *Nos2*, compared to the non-adhesive implant-tissue interface (Fig. 4c), consistent with the reduction in inflammatory cytokines in the adhesive implant-tissue interface on day 7 post-implantation as compared to day 3 post-implantation (Fig. 4d and Supplementary Table 1). Thus, the adhesive implant-tissue interface seems to induce a more robust pro-inflammatory neutrophil response than that of the non-adhesive implant-tissue interface on day 3 post-implantation, which is rapidly resolved by day 7 post-implantation.

Next, we performed bulk RNA sequencing of implant-abdominal wall interfaces for both adhesive and non-adhesive implants on days 3 and 14 post-implantation to further investigate gene-expression differences (Extended Data Fig. 8). Principal component analysis (PCA) shows separate clustering of samples for the non-adhesive and adhesive implant-tissue interfaces at each time point, indicating distinct transcriptomic profiles (Extended Data Fig. 8a,d). Differential gene expression analysis of the adhesive compared to the non-adhesive implant-tissue interface reveals 40 down-regulated and 33 up-regulated genes on day 3 post-implantation (Extended Data Figs. 8b and 9a). On day 14 post-implantation, 357 genes are down-regulated and 156 genes are upregulated (Extended Data Figs. 8e and 9b) in the adhesive implant-tissue interfaces as compared to the non-adhesive implant-tissue interface. On day 3 post-implantation, regulation of interferon production and striated muscle tissue development are enriched in the non-adhesive implant-tissue interface, indicating inflammatory and fibrosis processes, whereas cell proliferation and growth processes are enriched in the adhesive implant-tissue interface (Extended Data Fig. 8c). On day 14 post-implantation, fibrosis-associated processes are highly enriched in the non-adhesive implanttissue interface, such as muscle cell differentiation, myofibril assembly, and muscle structure development, whereas vasculature formation, neurogenesis, and proliferation are enriched in the adhesive implant-tissue interface (Extended Data Fig. 8f). These results again suggest reduced inflammatory response and rapid resolution of inflammation in the adhesive implant-tissue interface as compared to the non-adhesive implant-tissue interface.

To test our hypothesis in diverse animal models, we implanted the adhesive and non-adhesive implants on the abdominal wall surface of immunocompetent C57BL/6 mice and HuCD34-NCG humanized mice (Fig. 5a,c). Note that immunocompetent C57BL/6 mice are known to produce fibrosis and foreign body reactions similar to those observed in human patients<sup>32</sup>, while HuCD34-NCG humanized mice provide human-like immune responses<sup>33</sup>. Histological analysis shows that the adhesive implant-tissue interface exhibits no observable formation of the fibrous capsule, comparable to the native tissue on day 28 post-implantation in both C57BL/6 (Fig. 5b) and HuCD34-NCG (Fig. 5d) mouse models. In contrast, the non-adhesive implant-tissue interface shows substantial formation of the fibrous capsule in both models (Fig. 5b,d).

To further test our hypothesis in human-scale anatomy, we implanted the adhesive and non-adhesive implants in porcine models (Fig. 5e and Supplementary Fig. 5). Macroscopic observations demonstrate that the adhesive implant maintains stable integration with the surface of the porcine abdominal wall and small intestine on day 7 post-implantation in vivo (Extended Data Fig. 10). Histological analysis shows that the adhesive implant forms conformal integration with the tissue surface without observable formation of the fibrous capsule on the implant-tissue interface on day 7 post-implantation for both the abdominal wall (Fig. 5e) and small intestine (Extended Data Fig. 10a). In contrast, the non-adhesive implant-tissue interface exhibits substantial formation of the fibrous capsule (Fig. 5f and Extended Data Fig. 10b), in agreement with the observations in the rodent models.

To explore the potential utility of the adhesive anti-fibrotic interfaces, we demonstrated long-term in vivo electrophysiological recording and stimulation enabled by the implantable electrodes with the adhesive interface in a rat model for 84 days (Fig. 6). For continuous in vivo monitoring and modulation of the electrocardiogram, electrodes with either the adhesive or nonadhesive interface were implanted on the epicardial surface of animals for electrophysiological recording and stimulation on days 0, 3, 7, 14, 28, 56, and 84 post-implantation (Fig. 6a and Supplementary Fig. 6). Macroscopic observations showed that the electrodes with the adhesive interface maintained stable integration with the heart after 84 days of implantation in vivo (Fig. 6b). The amplitude of the R-wave recorded by the electrodes with the adhesive interface was consistently maintained throughout the study duration (84 days, Fig. 6e-g), whereas the R-wave amplitude recorded by the electrodes with the non-adhesive interface exhibited a substantial decrease over time (Fig. 6e). For electrophysical stimulation by the electrodes with the nonadhesive interface, the minimal stimulation current pulse amplitude needed to successfully pace the heart gradually increased until day 7 post-implantation and eventually failed to pace the heart on day 28 post-implantation (Fig. 6c). In contrast, the electrodes with the adhesive interface exhibited a consistent minimal stimulation current pulse amplitude for pacing and successfully maintained the capability to pace the heart for the duration of the study (84 days, Fig. 6d). These results are consistent with the histological findings from the tissues collected on day 28 postimplantation, where the electrodes with the non-adhesive interface showed encapsulation and physical separation from the epicardial surface by a thick fibrous capsule (Fig. 6h). In contrast, the electrodes with the adhesive interface showed conformal contact with the epicardial surface without observable formation of the fibrous capsule (Fig. 6i).

In this study, we demonstrated that the adhesive interface can not only provide conformal mechanical integration of the implant to the target tissue but also effectively mitigate the formation of the fibrous capsule on the adhesive implant-tissue interface by reducing the infiltration of inflammatory cells. The current work provides a promising strategy for long-term anti-fibrotic implant-tissue interfaces and offers valuable insights into implant-tissue interactions for future studies.

### References

- 1 Anderson, J. M. Biological responses to materials. *Annual Review of Materials Research* **31**, 81-110 (2001).
- Anderson, J. M., Rodriguez, A. & Chang, D. T. in *Seminars in Immunology*. 86-100 (Elsevier).
- Wick, G. et al. The immunology of fibrosis. Annual Review of Immunology **31**, 107-135 (2013).
- 4 Chandorkar, Y. & Basu, B. The foreign body response demystified. *ACS Biomaterials Science & Engineering* 5, 19-44 (2018).
- Harding, J. L. & Reynolds, M. M. Combating medical device fouling. *Trends in Biotechnology* **32**, 140-146 (2014).

- Yamagishi, K. *et al.* Tissue-adhesive wirelessly powered optoelectronic device for metronomic photodynamic cancer therapy. *Nature Biomedical Engineering* **3**, 27-36 (2019).
- Yang, Q. *et al.* Photocurable bioresorbable adhesives as functional interfaces between flexible bioelectronic devices and soft biological tissues. *Nature Materials* **20**, 1559-1570 (2021).
- Farra, R. *et al.* First-in-human testing of a wirelessly controlled drug delivery microchip. *Science Translational Medicine* **4**, 122ra121 (2012).
- Whyte, W. et al. Sustained release of targeted cardiac therapy with a replenishable implanted epicardial reservoir. *Nature Biomedical Engineering* **2**, 416-428 (2018).
- Feiner, R. & Dvir, T. Tissue–electronics interfaces: from implantable devices to engineered tissues. *Nature Reviews Materials* **3**, 17076 (2018).
- Yuk, H., Wu, J. & Zhao, X. Hydrogel interfaces for merging humans and machines. *Nature Reviews Materials* **7**, 935-952 (2022).
- Farah, S. *et al.* Long-term implant fibrosis prevention in rodents and non-human primates using crystallized drug formulations. *Nature Materials* **18**, 892-904 (2019).
- Gudipati, C. S., Finlay, J. A., Callow, J. A., Callow, M. E. & Wooley, K. L. The antifouling and fouling-release perfomance of hyperbranched fluoropolymer (HBFP)—poly (ethylene glycol)(PEG) composite coatings evaluated by adsorption of biomacromolecules and the green fouling alga Ulva. *Langmuir* 21, 3044-3053 (2005).
- Zhang, L. *et al.* Zwitterionic hydrogels implanted in mice resist the foreign-body reaction. *Nature Biotechnology* **31**, 553-556 (2013).
- 15 Xie, X. *et al.* Reduction of measurement noise in a continuous glucose monitor by coating the sensor with a zwitterionic polymer. *Nature biomedical engineering* **2**, 894-906 (2018).
- Bose, S. *et al.* A retrievable implant for the long-term encapsulation and survival of therapeutic xenogeneic cells. *Nature Biomedical Engineering* **4**, 814-826 (2020).
- Dolan, E. B. *et al.* An actuatable soft reservoir modulates host foreign body response. *Science Robotics* **4**, eaax7043 (2019).
- Whyte, W. *et al.* Dynamic actuation enhances transport and extends therapeutic lifespan in an implantable drug delivery platform. *Nature Communications* **13**, 4496 (2022).
- Noskovicova, N. *et al.* Suppression of the fibrotic encapsulation of silicone implants by inhibiting the mechanical activation of pro-fibrotic TGF-β. *Nature Biomedical Engineering* **5**, 1437-1456 (2021).
- Veiseh, O. *et al.* Size-and shape-dependent foreign body immune response to materials implanted in rodents and non-human primates. *Nature Materials* **14**, 643-651 (2015).
- Bochenek, M. A. *et al.* Alginate encapsulation as long-term immune protection of allogeneic pancreatic islet cells transplanted into the omental bursa of macaques. *Nature Biomedical Engineering* **2**, 810-821 (2018).
- Zhang, D. *et al.* Dealing with the foreign-body response to implanted biomaterials: strategies and applications of new materials. *Advanced Functional Materials* **31**, 2007226 (2021).
- Yuk, H. *et al.* Dry double-sided tape for adhesion of wet tissues and devices. *Nature* **575**, 169-174 (2019).
- Wu, J. *et al.* An off-the-shelf bioadhesive patch for sutureless repair of gastrointestinal defects. *Science Translational Medicine* **14**, eabh2857 (2022).

- Deng, J. *et al.* Electrical bioadhesive interface for bioelectronics. *Nature Materials* **20**, 229-236 (2021).
- Chen, X., Yuk, H., Wu, J., Nabzdyk, C. S. & Zhao, X. Instant tough bioadhesive with triggerable benign detachment. *Proceedings of the National Academy of Sciences* **117**, 15497-15503 (2020).
- Nam, S. & Mooney, D. Polymeric tissue adhesives. *Chemical Reviews* **121**, 11336-11384 (2021).
- Li, J. et al. Tough adhesives for diverse wet surfaces. Science 357, 378-381 (2017).
- Swartzlander, M. D. *et al.* Linking the foreign body response and protein adsorption to PEG-based hydrogels using proteomics. *Biomaterials* **41**, 26-36 (2015).
- Hedayati, M., Marruecos, D. F., Krapf, D., Kaar, J. L. & Kipper, M. J. Protein adsorption measurements on low fouling and ultralow fouling surfaces: a critical comparison of surface characterization techniques. *Acta Biomaterialia* **102**, 169-180 (2020).
- Saini, R. *et al.* Nitric oxide synthase localization in the rat neutrophils: immunocytochemical, molecular, and biochemical studies. *Journal of Leukocyte Biology* **79**, 519-528 (2006).
- Kolb, M. *et al.* Differences in the fibrogenic response after transfer of active transforming growth factor-β 1 gene to lungs of "fibrosis-prone" and "fibrosis-resistant" mouse strains. *American Journal of Respiratory Cell and Molecular Biology* **27**, 141-150 (2002).
- Doloff, J. C. *et al.* Identification of a humanized mouse model for functional testing of immune-mediated biomaterial foreign body response. *Science Advances* **9**, eade9488 (2023).

# **Data Availability**

All data supporting the findings of this study are available within the Article and its Supplementary Information. The RNA-seq data generated in the present study were deposited in the Gene Expression Omnibus (GEO) with accession number 'GSE198219'. Additional raw data generated in this study are available from the corresponding authors upon reasonable request.

## Acknowledgments

The authors thank the Koch Institute Swanson Biotechnology Center for technical support, specifically the Hope Babette Tang (1983) Histology Core for histological processing and the Peterson (1957) Nanotechnology Materials Core for TEM imaging, and Dr. Zhaohan Wei and Dr. Qing Zhou for insightful discussions. This work is supported by the National Institute of Health (1-R01-HL153857-01) and the National Science Foundation (EFMA-1935291).

## **Author contributions**

X.Z. proposed the idea. H.Y. developed the adhesive interface. J.W., H.Y., and X.Z. designed the method. J.W. and H.Y. performed the in vitro and in vivo rat studies. J.W. performed the in vivo mice studies. T.L.S. and L.G.G. performed the in vivo porcine study. J.D., J.W., and H.Y. performed the in vivo electrophysiological studies. J.W. performed the immunofluorescence and qPCR analyses. G.T. and A.V. performed the cytokines and sequencing analyses. R.T.B. evaluated the histological data. J.C. provided support for immunological analyses and edited the manuscript.

H.Y. and J.W. prepared figures with inputs from all authors. J.W., H.Y., X.Z. prepared the manuscript and all authors reviewed and edited the manuscript. H.Y. and X.Z. supervised the study.

# **Competing interests**

H.Y. and X.Z. have a financial interest in SanaHeal, Inc. X.Z. has a financial interest in SonoLogi, Inc. J.W., J.D., H.Y., and X.Z. are inventors of a patent application that covers the adhesive antifibrotic interfaces. Other authors declare no competing interests.

#### Methods

**Preparation of adhesive implants.** The adhesive layer of the adhesive implant was prepared using a previously reported method  $^{23,24}$ . To prepare an adhesive stock solution, 35 w/w % acrylic acid, 7 w/w % polyvinyl alcohol (PVA; Mw = 146,000-186,000, 99+% hydrolyzed), 0.2 w/w %  $\alpha$ -ketoglutaric acid, and 0.05 w/w % N, N-methylenebisacrylamide were added into nitrogen-purged deionized water. Next, 30 mg of acrylic acid N-hydroxysuccinimide ester was dissolved in each 1 ml of the above stock solution to prepare the adhesive precursor solution. The chitosan-based adhesive layer was prepared by replacing polyvinyl alcohol with 2 w/w% chitosan (Mw = 250-300 kDa, degree of deacetylation > 90 %; ChitoLytic). The precursor solution was poured onto a glass mold with a spacer (100- $\mu$ m thickness) and placed in a UV chamber (354 nm, 12 W power) for 30 min to prepare the adhesive hydrogel. The adhesive hydrogel was dried thoroughly under airflow and a vacuum desiccator to prepare the dry adhesive layer. A mock device of the adhesive implant was introduced by spin-coating a polyurethane resin (HydroThane, AdvanSource Biomaterials) onto the dry adhesive layer.

**Preparation of non-adhesive implants.** To prepare the non-adhesive implant, the adhesive implant was immersed in a sterile 1X PBS (pH 7.4, 144 mg L<sup>-1</sup> potassium phosphate monobasic, 9,000 mg L<sup>-1</sup> sodium chloride, and 795 mg L<sup>-1</sup> sodium phosphate dibasic) bath at room temperature overnight. During this process, the adhesive layer of the implant reached the equilibrium swollen state and became non-adhesive by losing the capability to form physical (hydrogen bonds) and covalent (amide bonds) crosslinking with tissues<sup>26</sup>.

Preparation of implantable electrodes. To prepare the implantable electrodes, gold electrodes (thickness, 50 μm) were integrated between the polyurethane layer (thickness, 100 μm) and the adhesive or non-adhesive layer (thickness, 100 μm) (Supplementary Fig. 6a). The surface of the gold electrode was treated with oxygen plasma for 3 min (30 W power, Harrick Plasma) to activate the surface functionalization, followed by immersion in cysteamine hydrochloride solution (50 mM in deionized water) for 1 h at room temperature. After the functionalization, the gold electrode was thoroughly washed with deionized water and dried with nitrogen flow. The functionalized gold electrode was cut into 2-mm diameter circles and placed on the adhesive hydrogel (two electrodes per implant). An electrode lead wire (AS633, Cooner Wire) was connected to the gold electrodes and the polyurethane insulation layer (HydroThane, AdvanSource Biomaterials) was introduced to the gold electrodes. The assembled implant was thoroughly dried under airflow and in a vacuum desiccator to prepare the adhesive implantable electrodes. To prepare the non-adhesive implantable electrodes were immersed in a sterile PBS bath overnight. All samples were prepared in an aseptic manner and were further disinfected under UV for 1 h before use.

**Mechanical characterizations.** Either the chitosan-based adhesive implant or the PVA-based adhesive implant was applied to ex vivo porcine skin with a gentle pressure for 5 s. Interfacial

toughness was measured based on the T-peel test (ASTM F2256). Shear strength was measured based on the lap-shear test (ASTM F2255). Tensile strength was measured based on the tensile test (ASTM F2258). All tests were conducted using a mechanical testing machine (2.5 kN load-cell, Zwick/Roell Z2.5). Aluminum fixtures were applied using cyanoacrylate glue to provide grips for tensile tests. All mechanical characterizations were performed 3 times using independently prepared samples.

In vitro protein adsorption assay. A gelatin hydrogel (10 w/v%, 300 g Bloom, Sigma-Aldrich) was used as the substrate for in vitro protein adsorption assay. The adhesive and non-adhesive implants were cut in 5-mm diameter circles by using a biopsy punch and placed on the gelatin hydrogel. The samples were then incubated in a solution with 5 mg ml<sup>-1</sup> fluorescently-tagged albumin (A13101, Thermo Fisher) or fibrinogen (F13191, Thermo Fisher) for 30 min. After the incubation, the samples were washed three times with fresh PBS to remove unadhered proteins. The samples were imaged using a confocal microscope (SP8, Leica), with the confocal plane set at the gelatin hydrogel-implant interface under a pitch model with excitation/emission at 495 nm/515 nm (for albumin) and 495nm/635 nm (for fibrinogen). The relative fluorescence intensity of absorbed proteins was calculated by using Image J (version 2.1.0).

In vivo intraperitoneal implantation in rat model. All animal studies on rats were approved by the MIT Committee on Animal Care, and all surgical procedures and postoperative care were supervised by the MIT Division of Comparative Medicine (DCM) veterinary staff.

Sprague-Dawley rats (Female and male, 225 to 250 g, 12 weeks, Charles River Laboratories) were used for all in vivo rat studies. Before implantation, all samples were prepared using aseptic techniques and were further disinfected for 1 h under UV light. For in vivo intraperitoneal implantation, the animals were anesthetized using isoflurane (2 to 3% isoflurane in oxygen) in an anesthetizing chamber before the surgery, and anesthesia was maintained using a nose cone throughout the surgery. Abdominal hair was removed, and the animals were placed on a heating pad during the surgery. The abdominal wall, colon, or stomach was exposed via a laparotomy. The adhesive implant (10 mm in width and 10 mm in length) was applied to the abdominal wall (n = 4 per time point), colon (n = 4), or stomach (n = 4) surface by gently pressing a surgical spatula or fingertip. The non-adhesive implant (10 mm in width and 10 mm in length) was implanted on the abdominal wall (n = 4 per time point), colon (n = 4), or stomach (n = 4)surface using sutures at the corners of the samples (8-0 Prolene, Ethicon). For commerciallyavailable tissue adhesives, 0.5 ml of Coseal (n = 6) or Tisseel (n = 6) was used to adhere the nonadhesive implant (10 mm in width and 10 mm in length) to the abdominal wall surface. For the adhesive implant with sutures, the adhesive implant (10 mm in width and 10 mm in length) was applied to the abdominal wall surface (n = 6), and sutures (8-0 Prolene, Ethicon) were used at the corners of the samples. The abdominal wall muscle and skin incisions were closed with sutures (4-0 Vicryl, Ethicon). On days 3, 7, 14, 28, and 84 post-implantation, the animals were euthanized using CO<sub>2</sub> inhalation. Abdominal wall, colon, or stomach tissues of interest were excised and fixed in 10 % formalin for 24 h for histological and immunofluorescence analysis. All animals in the study survived and were kept in normal health conditions based on daily monitoring by the MIT DCM veterinarian staff.

In vivo intrathoracic implantation in rat model. For in vivo intrathoracic implantation, the animals were anesthetized using isoflurane (2 to 3% isoflurane in oxygen) in an anesthetizing chamber before the surgery, and anesthesia was maintained using a nose cone throughout the surgery. Chest hair was removed, and endotracheal intubation was performed and connected to a mechanical ventilator (RoVent, Kent Scientific). The animals were placed on a heating pad for the duration of the surgery. The lung or heart was exposed via a thoracotomy. The pericardium was removed using fine forceps for the heart implantation. The adhesive implant (10 mm in width and 10 mm in length) was applied to the lung (n = 4) or heart (n = 4) surface by gently pressing a surgical spatula or fingertip. The non-adhesive implant (10 mm in width and 10 mm in length) was implanted to the lung (n = 4) or heart (n = 4) surface by sutures at the corners of the samples (8-0) Prolene, Ethicon). The muscle and skin incisions were closed with sutures (4-0 Vicryl, Ethicon). The animal was ventilated with 100 % oxygen until normal breathing resumed. On days 28 and 84 post-implantation, the animals were euthanized by CO<sub>2</sub> inhalation. Lung or heart tissues of interest were excised and fixed in 10 % formalin for 24 h for histological and immunofluorescence analysis. All animals in the study survived and were kept in normal health conditions based on daily monitoring by the MIT DCM veterinarian staff.

In vivo intraperitoneal implantation in mouse model. All animal studies on mice were approved by the MIT Committee on Animal Care, and all surgical procedures and postoperative care were supervised by the MIT DCM veterinary staff.

Immunocompetent C57BL/6 mice (Female and male, 18-25 g, 6-8 weeks, Jackson Laboratory) or humanized HuCD34-NCG mice (female, 18-25 g, 16-18 weeks, Charles River Laboratories) were anesthetized with 2-3% isoflurane, and then the abdomen was shaved and cleaned using betadine and 70% ethanol. A 1 cm incision was made along the abdomen midline and the abdominal wall was exposed via a laparotomy. The adhesive implant (5 mm in width and 5 mm in length) or non-adhesive implant (5 mm in width and 5 mm in length) was applied to the abdominal wall (n = 6 per group for C57BL/6 mice; n = 5 per group for HuCD34-NCG mice) by gently pressing. Both PVA-based and chitosan-based samples were used for C57BL/6 mice. Only PVA-based samples were used for HuCD34-NCG mice. The abdominal wall muscle and skin incisions were closed with sutures (5-0 Vicryl, Ethicon). On days 14 and 28 post-implantation, the abdominal wall of interest was excised and fixed in 10% formalin overnight for histological analysis.

In vivo intraperitoneal implantation in porcine model. All animal studies on pigs were approved by the Mayo Clinic institutional animal care and use committee (IACUC) at Rochester.

The female domestic pigs (female, 50 kg, 20 weeks, Manthei Hog Farm) were placed in dorsal recumbency, and the abdominal region was clipped and prepared aseptically. A blade was used to incise the ventral midline and extended using electrocautery when necessary. The linea alba was incised, and the peritoneum was bluntly entered, with the incision extended to match the skin incision. The small intestine was exteriorized and moist lap sponges were used for isolation. Then, the adhesive implant or non-adhesive implant was applied and adhered to the surface of the abdominal wall and small intestine (n = 4 for each group). The small intestine was thoroughly lavaged and returned to the abdomen. Then, the entire abdominal cavity was lavaged and suctioned, and the celiotomy incision was closed. On day 7 post-implantation, the animals were humanely euthanized, and the abdominal wall and small intestine of interest were excised and fixed in 10 % formalin for 24 h for histological analyses. All animals in the study survived and were kept in normal health condition based on daily monitoring by the Mayo Clinic Rochester veterinarian staff.

In vivo electrophysiological study. Before implantation, the adhesive and non-adhesive implantable electrodes were prepared using aseptic techniques and were further disinfected for 1h under UV. For in vivo epicardial electrode implantation, the animals were anesthetized using isoflurane (2 to 3% isoflurane in oxygen) in an anesthetizing chamber before the surgery, and anesthesia was maintained using a nose cone throughout the surgery. Chest and back hair were removed, and endotracheal intubation was performed, connecting the animals to a mechanical ventilator (RoVent, Kent Scientific). The animals were placed on a heating pad for the duration of the surgery. The heart was exposed via a thoracotomy and the pericardium was removed using fine forceps for the epicardial implantation. The adhesive implantable electrodes were applied to the left ventricular surface (n = 6) by gently pressing a surgical spatula or fingertip. The non-adhesive implantable electrodes were implanted to the left ventricular surface (n = 6) by sutures at the corners of the samples (8-0 Prolene, Ethicon). The lead wire was then tunneled subcutaneously from a ventral exit site close to the left fourth intercostal space to the dorsal side. The dorsal end of the lead wire was inserted through a subcutaneous port. The subcutaneous port was placed by interrupted sutures (4-0 Vicryl, Ethicon) between the shoulder blades of the animal and covered by a protective aluminum cap (VABRC, Instech Laboratories). The muscle and skin incisions were closed with sutures (4-0 Vicryl, Ethicon). The animal was ventilated with 100 % oxygen until autonomous breathing was regained.

On days 0, 3, 7, 14, 28, 56, and 84 post-implantation, each animal was anesthetized and connected to the data acquisition hardware (PowerLab, AD Instrument) and software (LabChart Pro 7, AD Instrument) for electrophysiological recording and stimulation by the implanted electrodes. For electrophysiological recording, the data acquisition hardware was connected to the implanted electrodes through the dorsal subcutaneous port. Epicardial signals were recorded to evaluate the R-wave amplitude. For electrophysiological stimulation, an external stimulator (FE180, AD Instrument) was connected to the implanted electrodes through the dorsal subcutaneous port. Unipolar rectangular current pulses (0.5 ms, 0-3 mA, 5-7 Hz) were used for

continuous ventricular pacing while the surface electrocardiogram (ECG) was monitored to evaluate the capture threshold. On days 28 and 84 post-implantation, the animals were euthanized by CO<sub>2</sub> inhalation. Heart tissues of interest were excised and fixed in 10 % formalin for 24 h for histological analysis. All animals in the study survived and were kept in normal health conditions based on daily monitoring by the MIT DCM veterinarian staff.

Immunofluorescence analysis. The expression of targeted markers (aSMA, CD68, CD3, CD206, iNOS, Vimentin, Neutrophil elastase) was analyzed after the immunofluorescence staining of the collected tissues. Before the immunofluorescence analysis, the paraffin-embedded fixed tissues were sliced and prepared into slides. The slides were deparaffinized and rehydrated with deionized water. Antigen retrieval was performed using the steam method during which the slides were steamed in IHC-Tek Epitope Retrieval Solution (IW-1100) for 35 min and then cooled for 20 min. Then the slides were washed in three changes of PBS for 5 min per cycle. After washing, the slides were incubated in primary antibodies 1:200 mouse anti-αSMA (ab7817, Abcam); 1:200 mouse anti-CD68 (ab201340, Abcam); 1:100 rabbit anti-CD3 (ab5690, Abcam); 1:1000 rabbit anti-CD206 (ab64693, Abcam); 1:500 mouse anti-vimentin (ab8978, Abcam); 1:2000 rabbit antiiNOS (ab283655, Abcam); 1:200 mouse anti-iNOS (GTX60599, GeneTex); 1:50 rabbit antineutrophil elastase (bs-6982R, Bioss) diluted with IHC-Tek Antibody Diluent for 1 h at room temperature. The slides were then washed three times in PBS and incubated with Alexa Fluor 488 labeled anti-rabbit or anti-mouse secondary antibody (1:200, Jackson Immunoresearch) or Alexa Fluor 594 labeled donkey anti-mouse secondary antibody (1:200, Jackson Immunoresearch) for 30 min. The slides were washed in PBS and then counterstained with propidium iodide solution for 20 min. A laser confocal microscope (SP8, Leica) was used for image acquisition. ImageJ (version 2.1.0) was used to quantify the number of cells in the collagenous layer at the implanttissue interface from the immunofluorescence images<sup>34</sup> (500 µm width of the field of view). All analyses were blinded with respect to the experimental conditions.

**Luminex quantitation analysis.** On days 1, 3, and 7 post-implantation, the abdominal muscle wall of interest was collected. The collected samples were snap-frozen in liquid nitrogen and homogenized on a TissueLyser LT (Qiagen) following the manufacturer's instructions. A Luminex multiplex assay was used to measure the concentrations of immune response-related cytokines and chemokines (RECYTMAG-65K, Milliplex). Values per sample were normalized to the total protein content and expressed as pg per total mg of protein, as provided in Supplementary Table 1.

**qPCR analysis.** RNA was isolated from the samples snap-frozen in liquid nitrogen immediately after excision using the TRIzol protocol (Invitrogen). All samples were homogenized and normalized by loading 1 μg of total RNA in all cases for reverse transcription using a SuperScript First Strand cDNA Synthesis Kit (Invitrogen). Complementary DNA (1:20 dilution) was amplified by qPCR with the following primers: *Mrc1* (5'-AACTTCATCTGCCAGCGACA-3'; reverse: 5'-

CGTGCCTCTTTCCAGGTCTT-3'), Tgfb1 (5'-AGTGGCTGAACCAAGGAGAC-3'; reverse: 5'-CCTCGACGTTTGGGACTGAT-3'), Nos2 (5'-TGGTGAGGGGACTGGACTTT-3'; reverse: 5'-CCAACTCTGCTGTTCTCCGT-3'), Cd86 (5'-AGACATGTGTAACCTGCACCAT-3'; reverse: 5'-TACGAGCTCACTCGGGCTTA-3'), S100a8 (5'-CGAAGAGTTCCTTGTGTTGGTG-3'; reverse: 5'-AGCTCTGTTACTCCTTGTGGC-3'), Ly6c (5'-ACCTGGTCACAGAGAGGAAGT-3'; 5'-AGCAGTTAGCATTAAGTGGGACT-3'), reverse: Il10TTGAACCACCCGGCATCTAC-3'; reverse: 5'-CCAAGGAGTTGCTCCCGTTA-3'), Cd11b (5'-GACTCCGCATTTGCCCTACT-3'; reverse: 5'-GCTGCCCACAATGAGTGGTA-3'), and glyceraldehyde-3-phosphate dehydrogenase (GAPDH) (5'-CACCATCTTCCAGGAGCGAG-3'; reverse: 5'-CCACGACATACTCAGCACCA-3'). Samples were incubated for 10 min at 95°C for 15 s and at 60°C for 1 min in the real-time cycler Agilent MX3000P. GAPDH was used as the reference gene for normalization and analysis. The comparative CT ( $\Delta\Delta$ CT) method was used for relative quantification of gene expression.

RNA-seq analysis. RNA extraction, library preparation, and sequencing reactions were conducted at GENEWIZ, LLC. Total RNA was extracted using the Qiagen RNeasy Plus Universal mini kit following the manufacturer's instructions (Qiagen). Extracted RNA samples were quantified using Qubit 2.0 Fluorometer (Life Technologies) and RNA integrity was checked on Agilent TapeStation 4200 (Agilent Technologies). RNA sequencing libraries were prepared using the NEBNext Ultra RNA Library Prep Kit for Illumina following the manufacturer's instructions (NEB). Briefly, mRNAs were first enriched with Oligo(dT) beads. Enriched mRNAs were fragmented for 15 min at 94 °C. First-strand and second-strand cDNAs were subsequently synthesized. cDNA fragments were end-repaired and adenylated at 3'ends, and universal adapters were ligated to cDNA fragments, followed by index addition and library enrichment by limitedcycle PCR. The sequencing libraries were validated on the Agilent TapeStation (Agilent Technologies), and quantified using Qubit 2.0 Fluorometer (Invitrogen) as well as by quantitative PCR (KAPA Biosystems). The sequencing libraries were clustered on 1 lane of a flow cell. After clustering, the flowcell was loaded on the Illumina HiSeq 4000 instrument and the samples were sequenced using a 2x150bp Paired End (PE) configuration. Image analysis and base calling were conducted by the HiSeq Control Software (HCS). Raw sequence data (.bcl files) generated from Illumina HiSeq were converted into fastq files and de-multiplexed using Illumina's bcl2fastq 2.17 software. One mismatch was allowed for index sequence identification.

Read quality was evaluated using FastQC, and data were pre-processed with Cutadapt<sup>35</sup> for adapter removal following best practices<sup>36</sup>. Gene expression against the mRatBN7.2 transcriptome (Ensembl release 104) <sup>37</sup> was quantified with STAR<sup>38</sup> and featureCounts<sup>39</sup>. Differential gene expression analysis was performed using DESeq2<sup>40</sup>, while ClusterProfiler<sup>41</sup> was utilized for functional enrichment investigations. Genes with log2 |Fold Change|  $\geq$ 1 and False Discovery Rate (FDR)  $\leq$  0.05 were considered statistically significant.

**Statistical analysis.** GraphPad Prism (version 9.2.0) was used to assess the statistical significance of all comparison studies in this work. Data distribution was assumed to be normal for all parametric tests, but not formally tested. In the statistical analysis for comparison between multiple groups, one-way ANOVA followed by Bonferroni's multiple comparison test was conducted with the significance threshold at \*P < 0.05, \*\* $P \le 0.01$ , \*\*\* $P \le 0.001$ , and \*\*\*\*P < 0.0001. In the statistical analysis of two groups, the two-sided unpaired t-test was used with the significance threshold at \*P < 0.05, \*\* $P \le 0.01$ , \*\*\* $P \le 0.001$ , and \*\*\*\*P < 0.0001.

#### **Additional References**

- Abràmoff, M. D., Magalhães, P. J. & Ram, S. J. Image processing with ImageJ. *Biophotonics international* **11**, 36-42 (2004).
- Martin, M. Cutadapt removes adapter sequences from high-throughput sequencing reads. *EMBnet. Journal* **17**, 10-12 (2011).
- Conesa, A. *et al.* A survey of best practices for RNA-seq data analysis. *Genome Biology* **17**, 13 (2016).
- Cunningham, F. et al. Ensembl 2019. Nucleic Acids Research 47, D745-D751 (2019).
- Dobin, A. et al. STAR: ultrafast universal RNA-seq aligner. Bioinformatics 29, 15-21 (2013).
- Liao, Y., Smyth, G. K. & Shi, W. featureCounts: an efficient general purpose program for assigning sequence reads to genomic features. *Bioinformatics* **30**, 923-930 (2014).
- Love, M. I., Huber, W. & Anders, S. Moderated estimation of fold change and dispersion for RNA-seq data with DESeq2. *Genome Biology* **15**, 550 (2014).
- Yu, G., Wang, L.-G., Han, Y. & He, Q.-Y. clusterProfiler: an R package for comparing biological themes among gene clusters. *Omics: A Journal of Integrative Biology* **16**, 284-287 (2012).

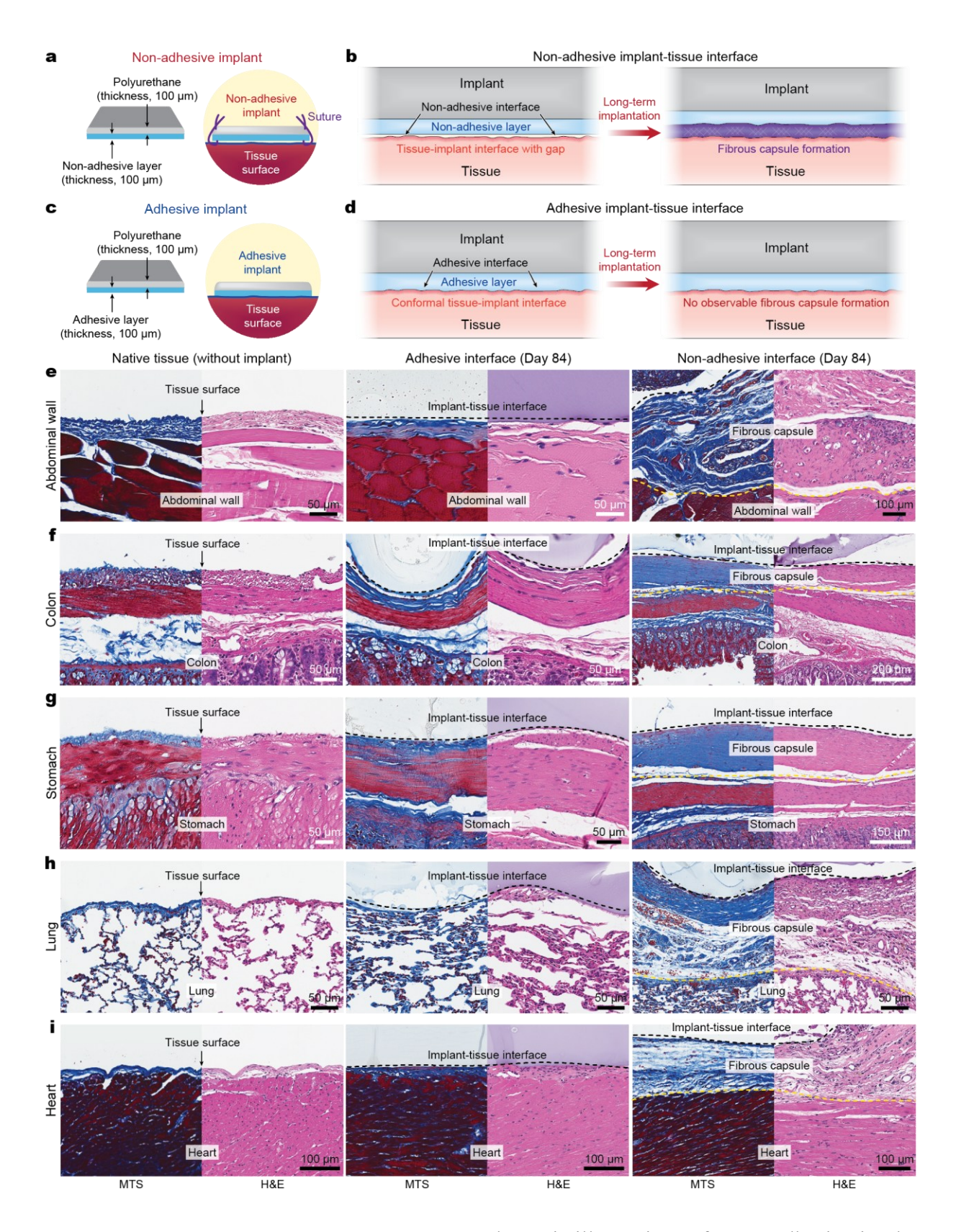


Fig. 1 | Adhesive anti-fibrotic interfaces. a,b, Schematic illustrations of a non-adhesive implant consisting of a mock device (polyurethane) and a non-adhesive layer (a) and long-term in vivo

implantation with fibrous capsule formation at the implant-tissue interface (b). **c**,**d**, Schematic illustrations of an adhesive implant consisting of the mock device (polyurethane) and an adhesive layer (c) and long-term in vivo implantation without observable fibrous capsule formation at the implant-tissue interface (d). **e-i**, Representative histology images stained with Masson's trichrome (MTS) and hematoxylin and eosin (H&E) for native tissue (left), the adhesive implant (middle), and non-adhesive implant (right) collected on day 84 post-implantation on the abdominal wall (e), colon (f), stomach (g), lung (h), and heart (i). Black and yellow dotted lines in the images indicate the implant-tissue interface and the fibrous capsule-tissue interface, respectively.

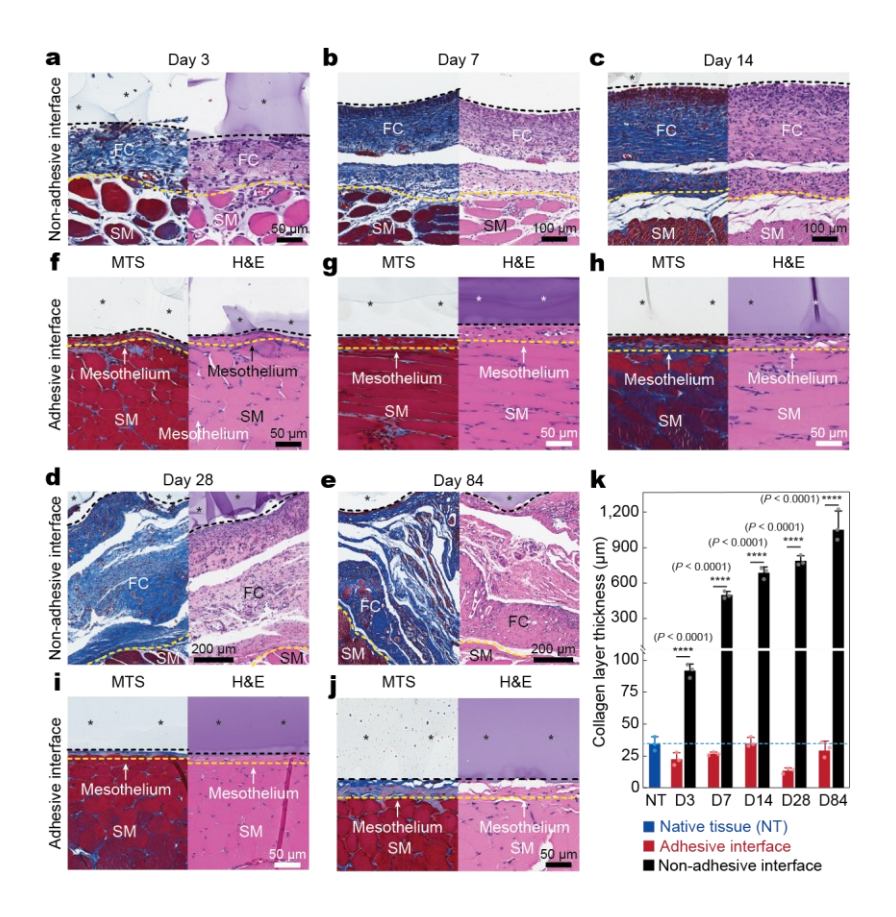


Fig. 2 | Histology analysis of the adhesive and non-adhesive implant-tissue interfaces at different time points. a-e, Representative histology images stained with Masson's trichrome (MTS, left) and hematoxylin and eosin (H&E, right) of the non-adhesive implant collected on day 3 (a), day 7 (b), day 14 (c), day 28 (d), and day 84 (e) post-implantation on the abdominal wall. f.j, Representative histology images stained with MTS (left) and H&E (right) of the adhesive implant collected on day 3 (f), day 7 (g), day 14 (h), and day 28 (i), and day 84 (j) post-implantation on the abdominal wall. \* in images indicates the implant; black dotted lines in images indicate the implant-tissue interface; yellow dotted lines in images indicate the mesothelium-fibrous capsule (non-adhesive implant) or the mesothelium-skeletal muscle (adhesive implant) interface. SM, skeletal muscle; FC, fibrous capsule. k, Collagen layer thickness at the implant-tissue interface measured at different time points post-implantation. The blue dotted line indicates the average collagen layer thickness of the native tissue. Values in k represent the mean and the standard deviation (n = 3 implants; independent biological replicates). Statistical significance and P values are determined by two-sided unpaired t-tests; \*\*\*\*P < 0.0001.

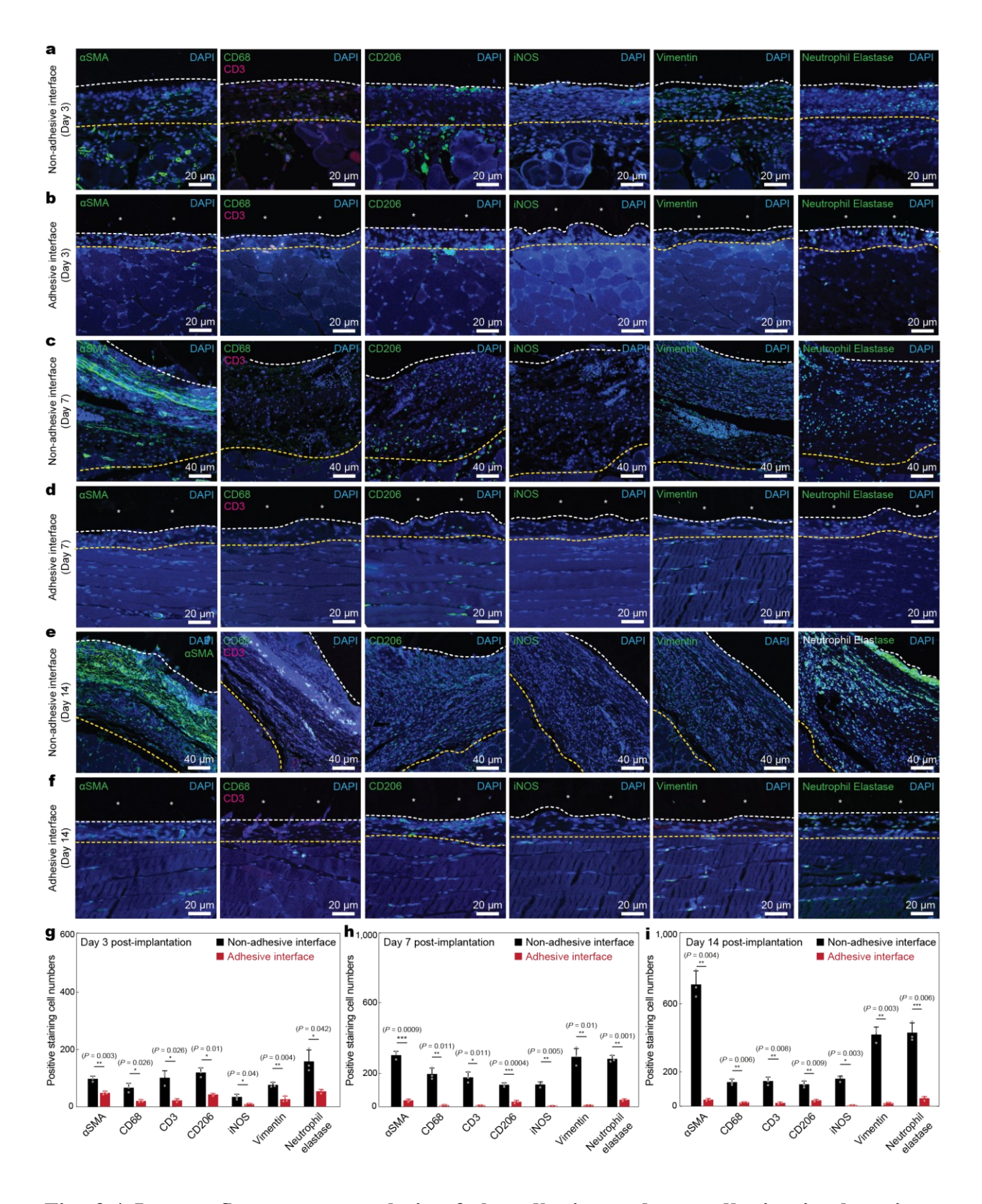


Fig. 3 | Immunofluorescence analysis of the adhesive and non-adhesive implant-tissue interfaces at different time points. a,c,e, Representative immunofluorescence images of the non-

adhesive implant collected on day 3 (a), day 7 (c), and day 14 (e) post-implantation on the abdominal wall. **b,d,f**, Representative immunofluorescence images of the adhesive implant collected on day 3 (b), day 7 (d), and day 14 (f) post-implantation on the abdominal wall. In immunofluorescence images, cell nuclei are stained with 4',6-diamidino-2-phenylindole (DAPI, blue); green fluorescence corresponds to the expression of fibroblast ( $\alpha$ SMA), neutrophil (Neutrophil elastase), and macrophage (CD68, Vimentin, CD206, iNOS); red fluorescence corresponds to the expression of T cell (CD3). \* in images indicates the implant; white dotted lines in images indicate the implant-tissue interface; yellow dotted lines in images indicate either the mesothelium-fibrous capsule interface (non-adhesive implant) or the mesothelium-skeletal muscle interface (adhesive implant). **g-i**, Quantification of cell numbers in the collagenous layer at the implant-tissue interface over a representative width of 500 $\mu$ m from the immunofluorescence images on day 3 (g), day 7 (h), and day 14 (i) post-implantation. Values in **g-i** represent the mean and the standard deviation (n = 3 implants; independent biological replicates). Statistical significance and P values are determined by two-sided unpaired t-tests; ns, not significant; \*P < 0.05; \*\* $P \le 0.01$ ; \*\*\* $P \le 0.001$ ; \*\*\*\* $P \le 0.001$ ; \*\*\*\* $P \le 0.001$ .

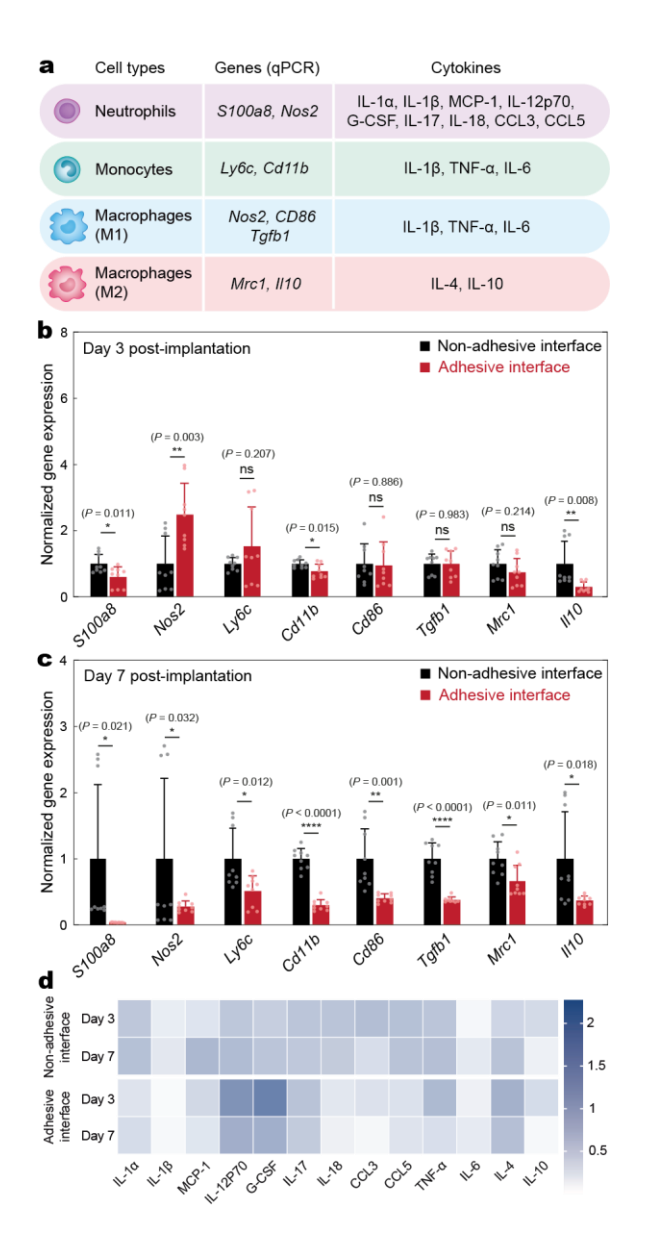
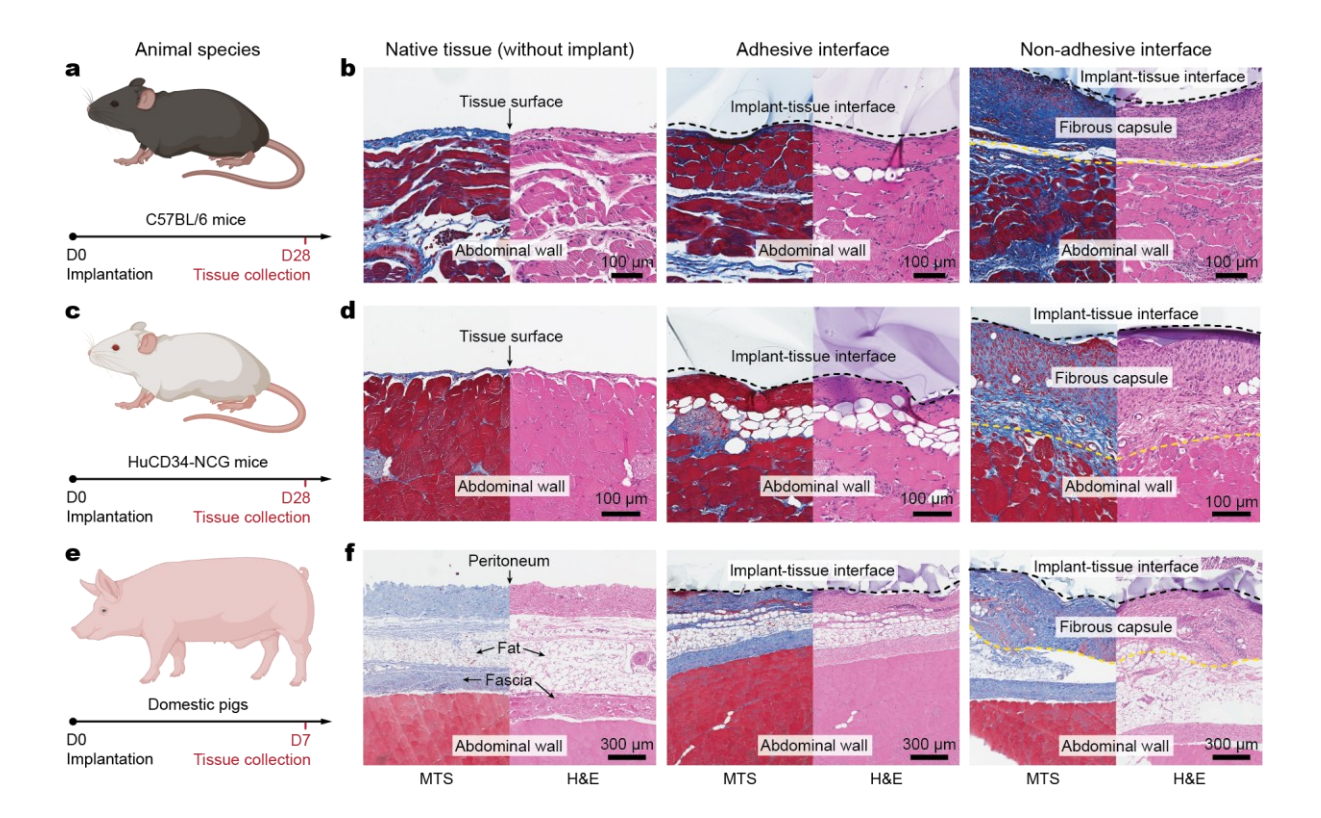


Fig. 4 | Q-PCR and Luminex analysis of the adhesive and non-adhesive implant-tissue interfaces. a, Genes and cytokines relevant to each cell type in the q-PCR and Luminex studies. b-c, Normalized gene expression of immune cell-related markers for the non-adhesive and the adhesive implant-tissue interface collected on day 3 (b) and day 7 (c) post-implantations on the abdominal wall. d, Heatmap of immune cell-related cytokines measured with Luminex assay of the non-adhesive and the adhesive implant-tissue interfaces collected on days 3 and 7 post-implantations on the abdominal wall. Values in b,c represent the mean and the standard deviation (n = 9 implants; independent biological replicates). Statistical significance and P values are determined by two-sided unpaired t-tests; ns, not significant;  $*P < 0.05; **P \le 0.01; ***P \le 0.001; ****P < 0.0001.$ 



**Fig. 5** | **Adhesive anti-fibrotic interfaces in diverse animal models. a,c,e**, Schematic illustrations for the study design in C57BL/6 mice (a), HuCD34-NCG humanized mice (c), and pigs (e). Implants are placed on the abdominal wall of the animals. **b,d,f**, Representative histology images stained with Masson's trichrome (MTS) and hematoxylin and eosin (H&E) for native tissue (left), adhesive implant (middle), and non-adhesive implant (right) collected on day 28 post-implantation in C57BL/6 mice (b) and in HuCD34-NCG humanized mice (d), and on day 7 post-implantation in pigs (f). Black dotted lines in images indicate the implant-tissue interface; yellow dotted lines in images indicate the fibrous capsule-tissue interface. Parts of **a,c,e** were created with BioRender.com.

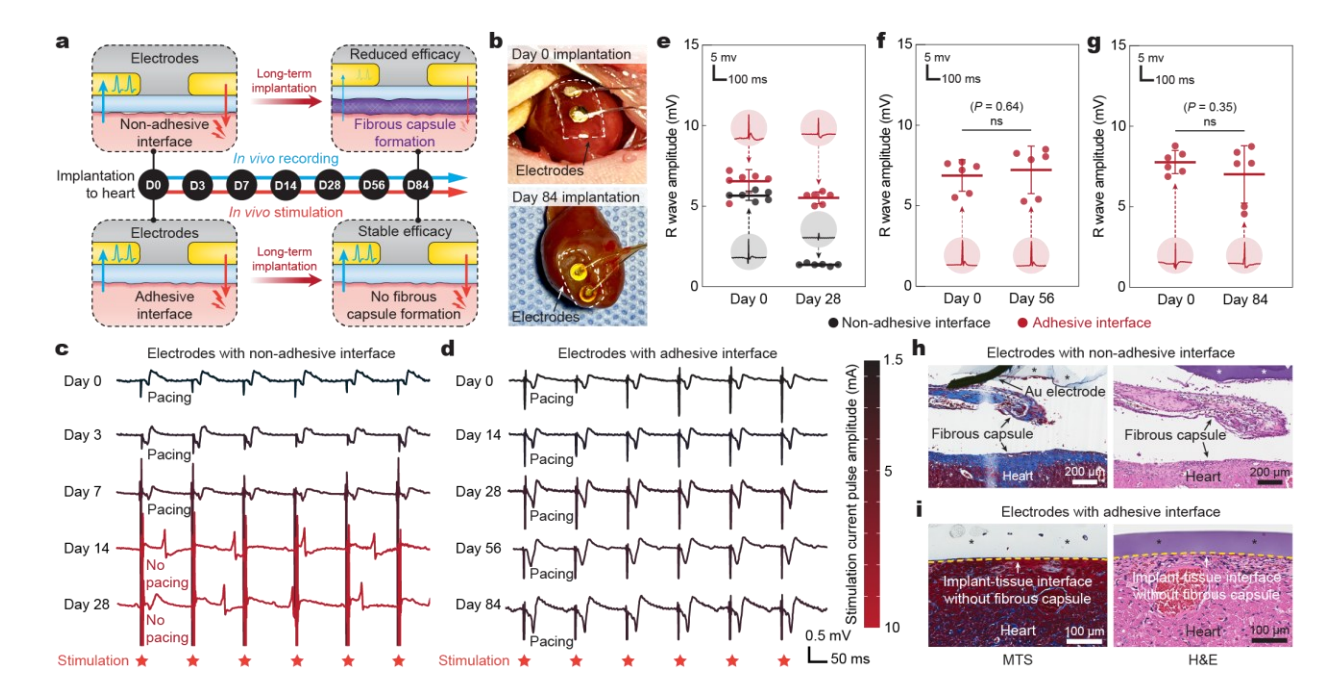
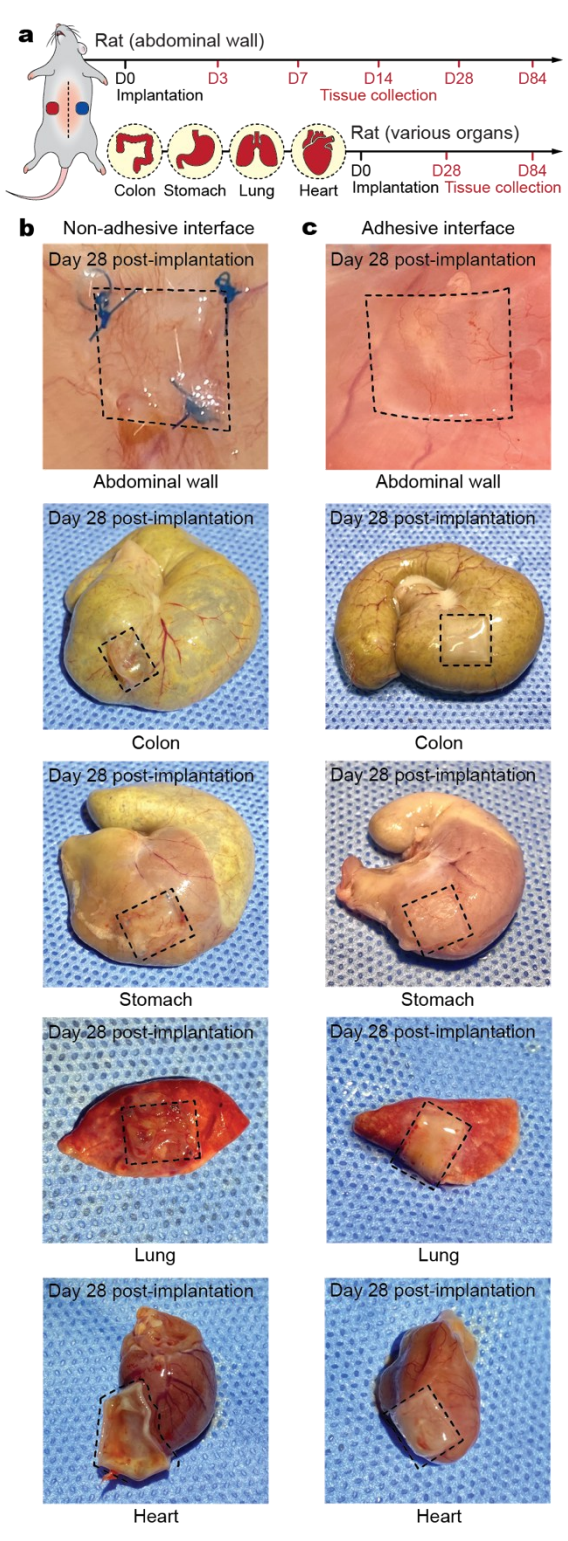
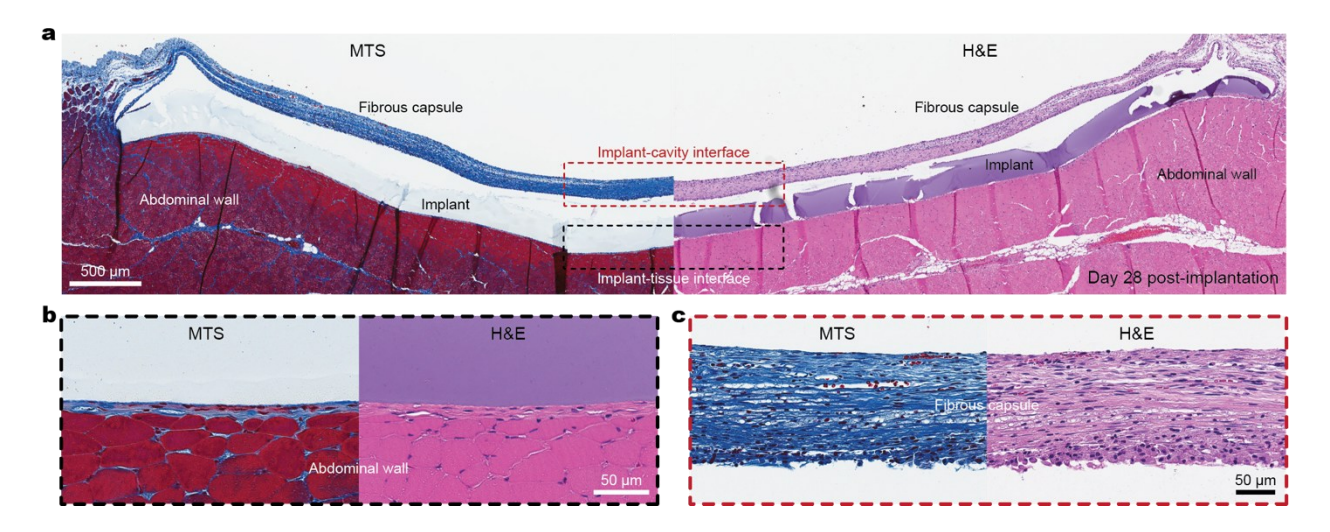


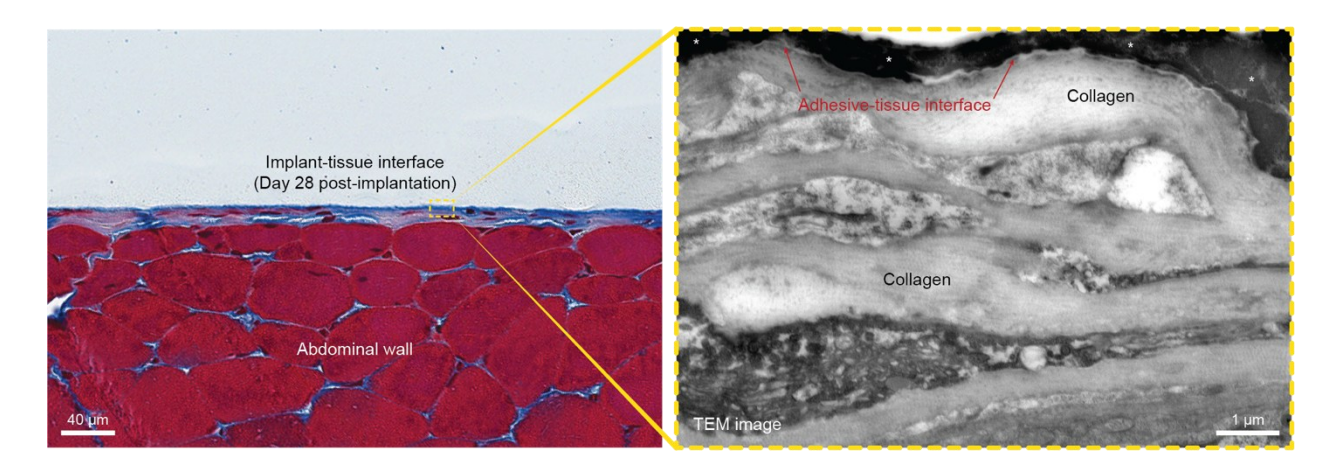
Fig. 6 | Long-term in vivo bi-directional electrical communication via the adhesive antifibrotic interfaces. a, Schematic illustrations for the in vivo electrophysiological recording and stimulation via implanted electrodes with the non-adhesive or the adhesive implant-tissue interfaces. b, Photographs of the heart collected on days 0 and 84 post-implantation for electrodes with the adhesive interface. White dotted lines in photographs indicate the boundary of implants. c, Representative epicardial electrocardiograms after stimulation via implanted electrodes with the non-adhesive implant-tissue interface on days 0, 3, 7, 14, and 28 post-implantation on a rat heart. d, Representative epicardial electrocardiograms after stimulation via implanted electrodes with the adhesive implant-tissue interface on days 0, 14, 28, 56, and 84 post-implantation on a rat heart. eg, Recorded R-wave amplitude via implanted electrodes with the non-adhesive (black) and the adhesive (red) implant-tissue interfaces on day 28 (e), day 56 (f), and day 84 (g) post-implantation on a rat heart. Inset plots show representative recorded waveforms. h,i, Representative histology images stained with Masson's trichrome (MTS, left) and hematoxylin and eosin (H&E, right) of the electrodes with non-adhesive (h) and the adhesive (i) implant collected on day 28 postimplantation on a rat heart. \* in images indicates the implant; yellow dotted lines in images indicate the implant-tissue interface. Values in e-g represent the mean and the standard deviation (n = 6animals; independent biological replicates). Statistical significance and P values are determined by two-sided unpaired *t*-tests; ns, not significant.



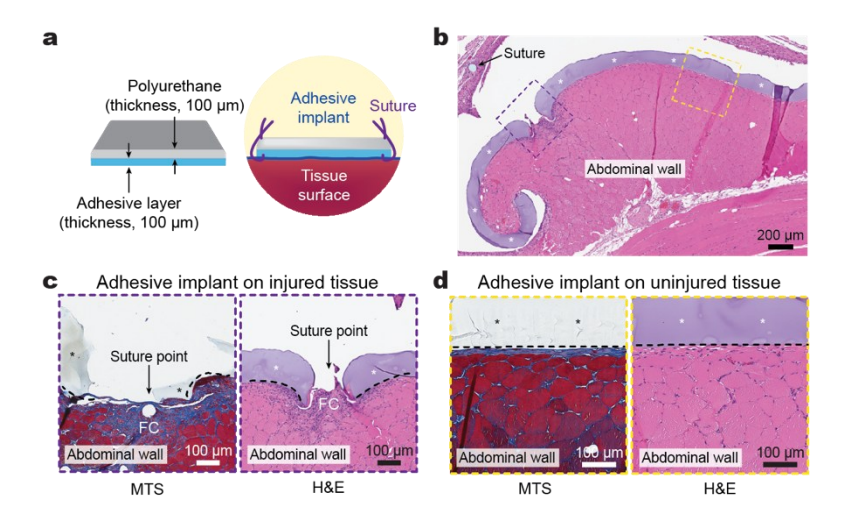
Extended Data Fig. 1 | In vivo implantation of the adhesive and non-adhesive implants to various organs. a, Schematic illustrations for the in vivo rat studies. b,c, Photographs of various organs collected on day 28 post-implantation for the non-adhesive implant (b) and the adhesive implant (c). Black dotted lines in photographs indicate the boundary of implants.



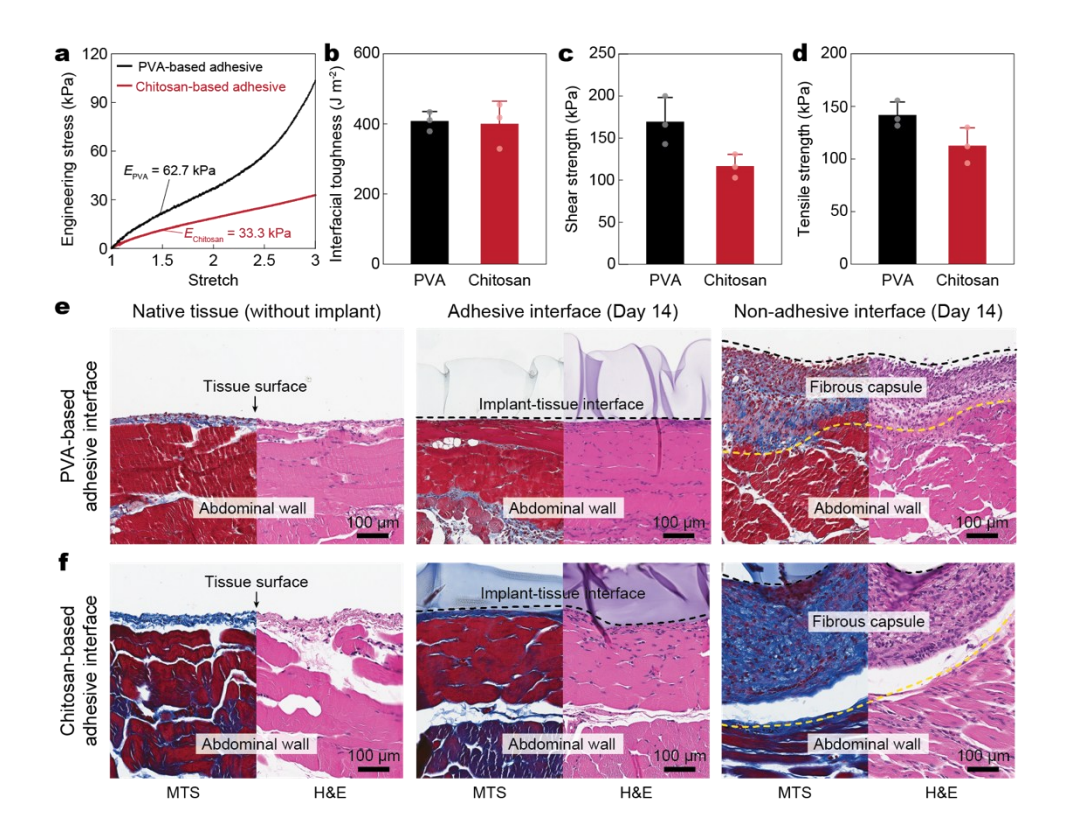
Extended Data Fig. 2 | Adhesive implant histology. a, Representative histology images stained with Masson's trichrome (MTS, left) and hematoxylin and eosin (H&E, right) of the adhesive implant collected on day 28 post-implantation to the abdominal wall. Black and red dotted areas indicate the implant-tissue interface and the implant-abdominal cavity interface, respectively. b,c, Representative histology images stained with MTS (left) and H&E (right) of the implant-tissue interface (b) and implant-cavity interface (c) for the adhesive implant collected on day 28 post-implantation to the abdominal wall.



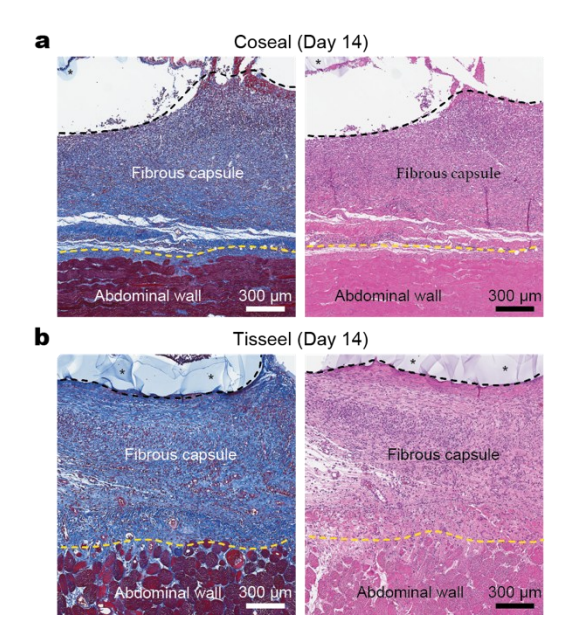
**Extended Data Fig. 3** | **TEM image of the adhesive implant-tissue interface.** Representative histology image stained with Masson's trichrome (left) and TEM image (right) of the adhesive implant collected on day 28 post-implantation to the abdominal wall. \* in images indicates the implant.



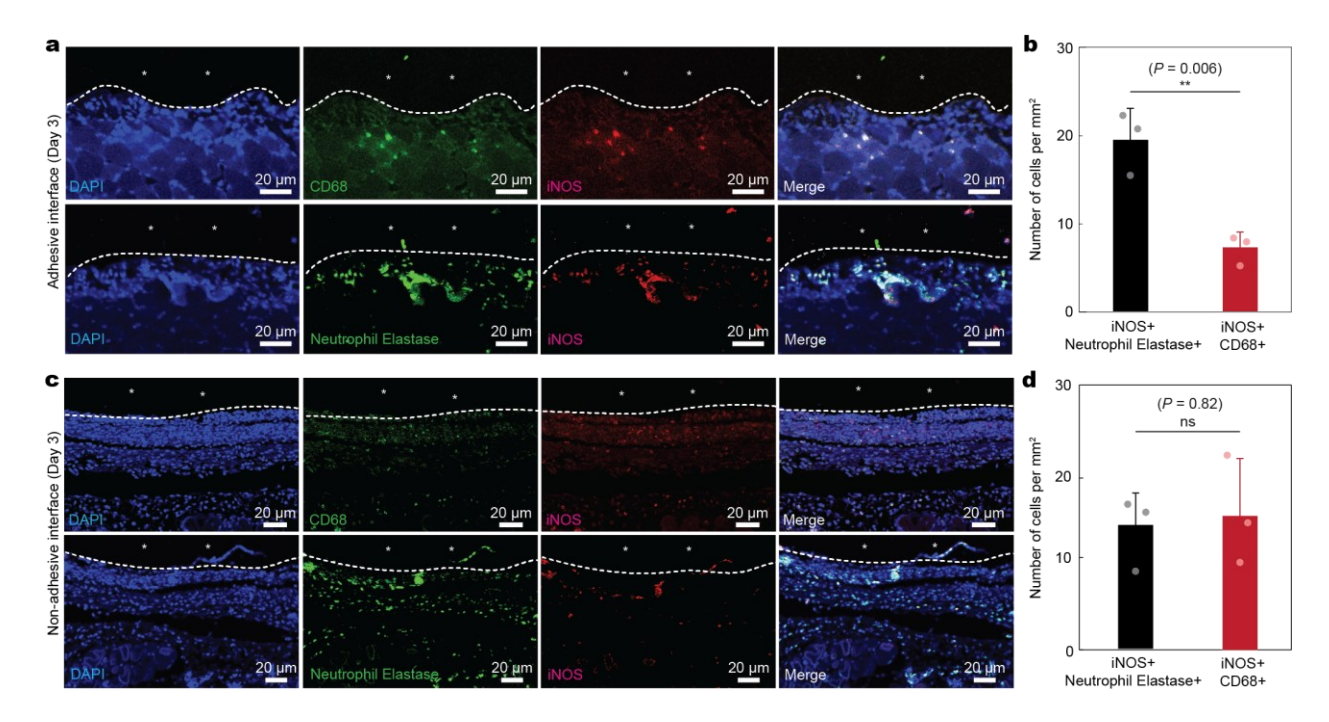
**Extended Data Fig. 4** | **Adhesive implant-tissue interface with sutures. a**, Schematic illustrations of the adhesive implant with sutures at the corners. **b**, Representative histology image stained with hematoxylin and eosin (H&E) for the adhesive implant with sutures on the abdominal wall collected on day 28 post-implantation. **c,d**, Representative histology images stained with Masson's trichrome (MTS, left) and H&E (right) for the suture point (c) and the intact adhesive-tissue interface (d) collected on day 28 post-implantation to the abdominal wall. \* in images indicates the implant; black dotted lines indicate the implant-tissue interface. FC, fibrous capsule.



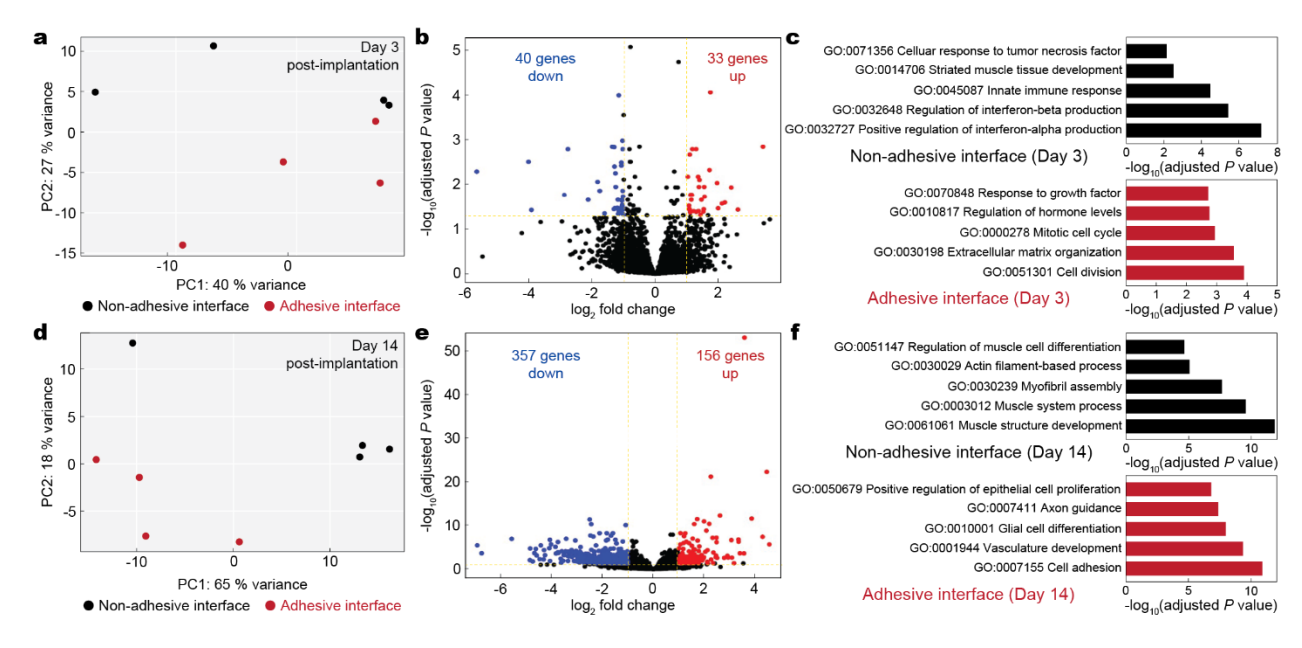
**Extended Data Fig. 5** | **Chitosan-based adhesive interface. a**, Engineering stress vs. stretch curves for the PVA-based and chitosan-based adhesive interfaces.  $E_{PVA}$ , Young's modulus of the PVA-based adhesive interface;  $E_{chitosan}$ , Young's modulus of the chitosan-based adhesive interface. **b-d**, Interfacial toughness (b), shear strength (c), and tensile strength (d) of the PVA-based and chitosan-based adhesive interfaces on ex vivo porcine skin. **e,f**, Representative histology images stained with Masson's trichrome (MTS) and hematoxylin and eosin (H&E) for native tissue (left), adhesive implant (middle), and non-adhesive implant (right) collected on day 14 post-implantation to the abdominal wall based on the PVA-based adhesive interface (e) and the chitosan-based adhesive interface (f). Black and yellow dotted lines in the images indicate the implant-tissue interface and the fibrous capsule-tissue interface, respectively. Values in **b-d** represent the mean and the standard deviation (n = 3, independent samples).



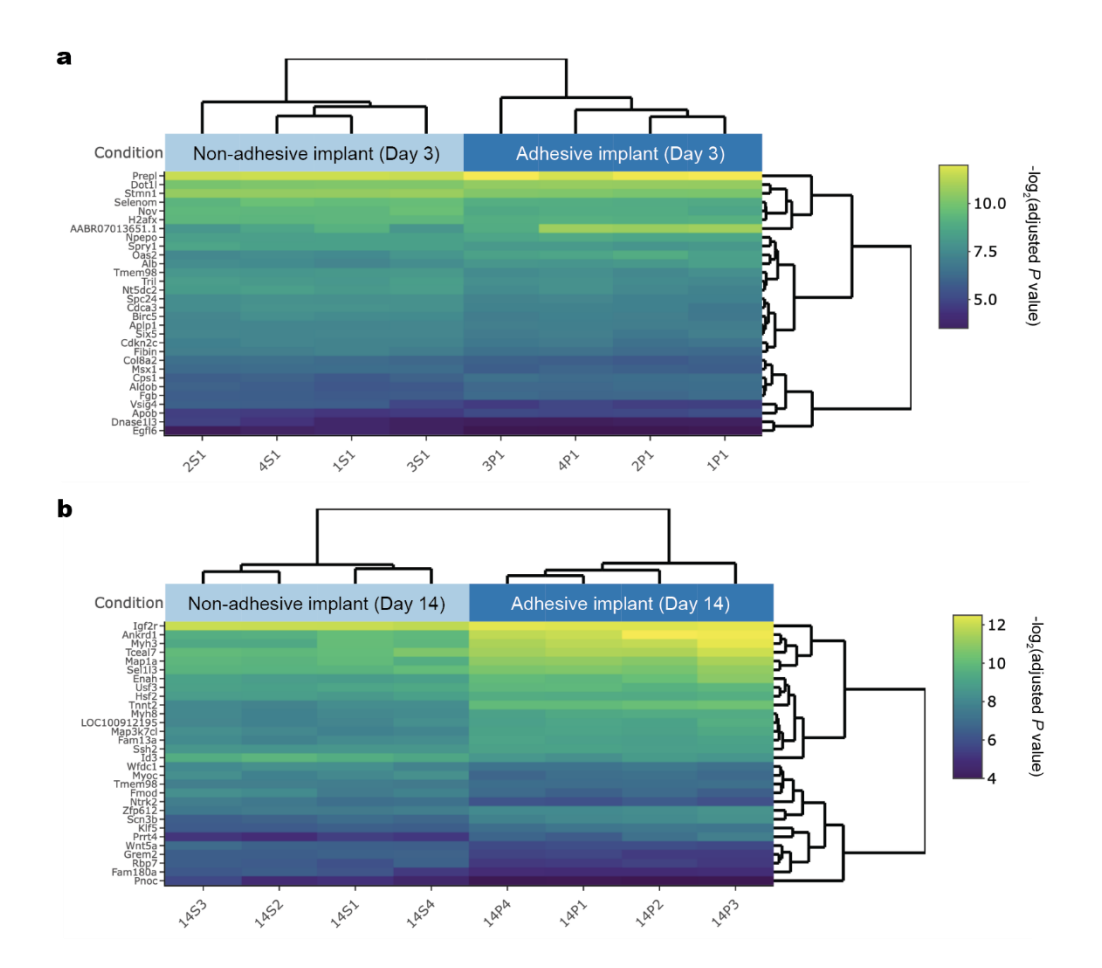
Extended Data Fig. 6 | Adhesive interface by commercially-available tissue adhesives. a,b, Representative histology images stained with Masson's trichrome (left) and hematoxylin and eosin (right) for the implant integrated to the abdominal wall surface by Coseal (a) and Tisseel (b) collected on day 14 post-implantation. \* in images indicates the implant; black dotted lines indicate the implant-tissue interface; yellow dotted lines indicate the fibrous capsule-tissue interface.



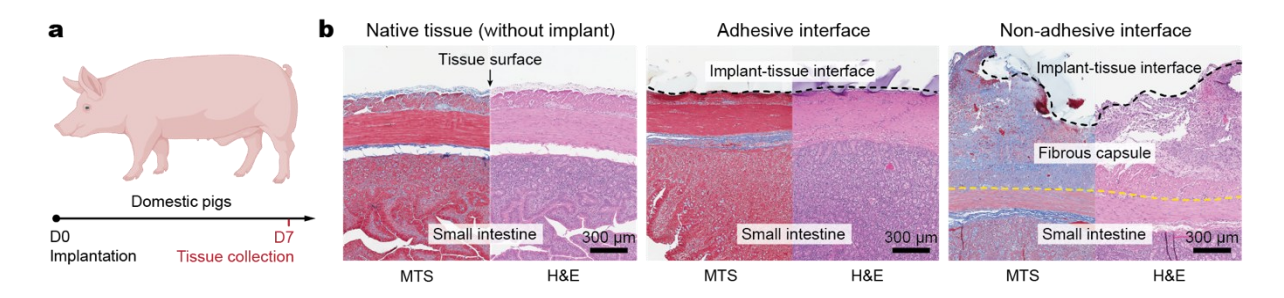
Extended Data Fig. 7 | Immunofluorescence analysis of iNOS+ cells at the implant-tissue interface. a, Representative immunofluorescence images at the adhesive implant-tissue interface on day 3 post-implantation to the abdominal wall. b, Quantification of iNOS+/Neutrophil Elastase+ and iNOS+/CD68+ cells per unit area on day 3 post-implantation for the adhesive implant-tissue interface. c, Representative immunofluorescence images at the non-adhesive implant-tissue interface on day 3 post-implantation to the abdominal wall. d, Quantification of iNOS+/Neutrophil Elastase+ and iNOS+/CD68+ cells per unit area on day 3 post-implantation for the non-adhesive implant-tissue interface. In immunofluorescence images, cell nuclei are stained with 4',6-diamidino-2-phenylindole (DAPI, blue); green fluorescence corresponds to the expression of macrophage (CD68) and neutrophil (Neutrophil Elastase); red fluorescence corresponds to the expression of iNOS. \* in images indicates the implant; white dotted lines in images indicate the implant-tissue interface. Values in b,d represent the mean and the standard deviation (n = 3 implants; independent biological replicates). Statistical significance and P values are determined by two-sided unpaired t-tests; ns, not significant; \*\* $P \le 0.01$ .



Extended Data Fig. 8 | Transcriptomic analysis of adhesive and non-adhesive implant-tissue interfaces. a, Principal component analysis (PCA) plot illustrating the variances of the adhesive (red dots, n = 4) and non-adhesive (black dots, n = 4) implant-tissue interface dataset collected on day 3 post-implantation to the abdominal wall. b, Volcano plot displaying the gene expression profiles for the non-adhesive and adhesive implant-tissue interfaces collected on day 3 postimplantation to the abdominal wall. Colored (blue and red) data points represent genes that meet the threshold of fold change (FC) above 1 or under -1, False Discovery Rate (FDR) < 0.05. Blue and red colored dots indicate down- and up-regulated genes in the adhesive implant-tissue interface compared to the non-adhesive implant-tissue interface, respectively. c, Top 5 enriched processes from Gene Ontology (GO) enrichment analysis of differentially expressed genes in the nonadhesive (black) and adhesive (red) implant-tissue interfaces collected on day 3 post-implantation to the abdominal wall. **d**, PCA plot illustrating the variances of the adhesive (red dots, n = 4) and non-adhesive (black dots, n = 4) implant-tissue interface dataset collected on day 14 postimplantation to the abdominal wall. e, Volcano plot displaying the gene expression profiles for the non-adhesive and adhesive implant-tissue interfaces collected on day 14 post-implantation to the abdominal wall. Colored (blue and red) data points represent genes that meet the threshold of fold change (FC) above 1 or under -1, False Discovery Rate (FDR) < 0.05. Blue and red colored dots indicate down- and up-regulated genes in the adhesive implant-tissue interface compared to the non-adhesive implant-tissue interface, respectively. f, Top 5 enriched processes from Gene Ontology (GO) enrichment analysis of differentially expressed genes in the non-adhesive (black) and adhesive (red) implant-tissue interfaces collected on day 14 post-implantation to the abdominal wall.



**Extended Data Fig. 9** | **Visualization of RNA sequencing results. a,b**, Bi-clustering heatmap to visualize the expression profiles of the top 30 differentially expressed genes sorted by their adjusted *P* value by plotting their log2 transformed expression values in samples day 3 (a) and day 14 (b) post-implantation. Dendrograms were drawn from Ward hierarchical clustering.



**Extended Data Fig. 10** | **Adhesive anti-fibrotic interfaces in porcine model. a**, Schematic illustration for the study design based on the porcine model. **b**, Representative histology images stained with Masson's trichrome (MTS) and hematoxylin and eosin (H&E) for native tissue (left), adhesive implant (middle), and non-adhesive implant (right) collected on 7 days post-implantation to the small intestine. Black dotted lines in images indicate the implant-tissue interface; yellow dotted lines in images indicate the fibrous capsule-tissue interface. Parts of **a** were created with BioRender.com.